The Astrophysical Journal, 693:8–22, 2009 March 1 doi:10.1088/0004-637X/693/1/8

HIGH-REDSHIFT QUASARS IN THE COSMOS SURVEY: THE SPACE DENSITY OF $z > 3$ X-RAY SELECTED QSOs

M. Brusa[1], A. Comastri[2], R. Gilli[2], G. Hasinger[1], K. Iwasawa[2,1], V. Mainieri[3], M. Mignoli[2], M. Salvato[4], G. Zamorani[2], A. Bongiorno[1], N. Cappelluti[1], F. Civano[5], F. Fiore[6], A. Merloni[1,7], J. Silverman[8], J. Trump[9], C. Vignali[10], P. Capak[4], M. Elvis[5], O. Ilbert[11], C. Impey[9], and S. Lilly[8]

[1] Max Planck Institut für Extraterrestrische Physik, Giessenbachstrasse, 1, D-85748, Garching bei Muenchen, Germany
[2] INAF–Osservatorio Astronomico di Bologna, via Ranzani 1, I–40127 Bologna, Italy
[3] European Southern Observatory, Karl-Schwarzschild-str. 2, 85748 Garching bei München, Germany
[4] California Institute of Technology, MC 105-24, 1200 East California Boulevard, Pasadena, CA 91125, USA
[5] Harvard-Smithsonian Center for Astrophysics, 60 Garden Street, Cambridge, MA 02138, USA
[6] INAF–Osservatorio Astronomico di Roma, via Frascati 33, Monteporzio-Catone (Roma), I-00040, Italy
[7] Excellence Cluster Universe, Boltzmannstrasse 2, D-85748, Garching bei Muenchen, Germany
[8] Institute of Astronomy, Swiss Federal Institute of Technology (ETH Hönggerberg), CH-8093, Zürich, Switzerland
[9] Steward Observatory, University of Arizona, 933 North Cherry Avenue, Tucson, AZ 85 721, USA
[10] Dipartimento di Astronomia Universitá di Bologna, via Ranzani 1, I–40127 Bologna, Italy
[11] University of Hawaii, 2680 Woodlawn Dr., Honolulu, HI, 96822, USA

Received 2008 May 16; accepted 2008 October 28; published 2009 February 27

ABSTRACT

We present a new measurement of the space density of high-redshift ($z \simeq 3.0$–4.5), X-ray-selected quasi-stellar objects (QSOs) obtained by exploiting the deep and uniform multiwavelength coverage of the COSMOS survey. We have assembled a large (40 objects), homogeneous sample of $z > 3$ QSOs with X-ray flux $F_{0.5-2\,\mathrm{keV}} > 10^{-15}$ erg cm^{-2} s^{-1}, and available spectroscopic (22) or photometric (18) redshifts. We discuss their optical (color–color diagrams) and X-ray properties, their number counts and space densities and compare our findings with previous works and model predictions. We find that the optical properties of X-ray-selected quasars are not significantly different from those of optically selected samples. There is evidence for substantial X-ray absorption ($\log N_H > 23$ cm^{-2}) in about 20% of the sources in the sample. We find that the comoving space density of luminous ($L_X \gtrsim 10^{44}$ erg s^{-1}) QSOs declines exponentially (by an e-folding per unit redshift) in the $z \sim 3.0$–4.5 range, with a behavior similar to that observed for optically bright unobscured QSOs selected in large area optical surveys. Prospects for future, large and deep X-ray surveys are also discussed.

Key words: galaxies: active – surveys – X-rays: galaxies

Online-only material: color figures

1. INTRODUCTION

The well known correlations observed in the local universe between super massive black holes (SMBHs) and galaxy properties such as bulge luminosity and stellar velocity dispersion (Gebhardt et al. 2000; Ferrarese & Merrit 2000), point toward a tight link between the assembly of the bulge mass and the SMBH. The high-redshift active galactic nucleus (AGN) luminosity function (LF) and the source counts represent key observational constraints for theoretical models of galaxy and SMBH formation and evolution. While most models are reasonably successful in reproducing several observables in the high-luminosity regime (Di Matteo et al. 2005; Volonteri & Rees 2006; Hopkins et al. 2005; Lapi et al. 2006; Menci et al. 2008), they have to face the paucity of data, especially at high redshifts and low luminosities. Given that theoretical predictions are used to determine key physical parameters, such as the quasi-stellar object (QSO) duty cycle, the BH seed mass function, and the accretion rates, a reliable observational estimate of the QSO LF and evolution at high redshift is extremely important.

Large optical surveys, most notably the 2dF Quasar Redshift Survey (2QZ; Croom et al. 2005) and the Sloan Digital Sky Survey (SDSS; i.e., Richards et al. 2006) were able to accurately measure the shape of the LF up to $z \sim 2.0$–2.5 and to constrain the bright ($M_B < -25.5$ or $M_I < -27.6$, corresponding to bolometric luminosities of $\log L_{\mathrm{bol}} \gtrsim 46$ erg s^{-1}) QSO LF up to $z \sim 6.5$: the space density of optically selected QSO peaks at $z \sim 2$–3 and decreases approximately by a factor of 3 per unit redshift in the range $z \simeq 3$–6 (Schmidt et al. 1995; Fan et al. 2001, 2004; Richards et al. 2006). These high-redshift quasar surveys, however, are relatively shallow and probe only the bright end of the LF. Recently, deep optical surveys were able to probe the LF at significantly fainter magnitudes using different selection criteria (e.g., Wolf et al. 2003; Hunt et al. 2004; Fontanot et al. 2007; Bongiorno et al. 2007; Siana et al. 2008). However, the statistics on the faint QSO population at $z > 3$ is still limited given the typically small areas surveyed.

Moreover, optically selected quasars are known to make up only a fraction of the entire population of accreting SMBHs: not only is most of the accretion power in the universe obscured by large amounts of dust and gas (see e.g., Fabian & Iwasawa 1999), but also AGNs and QSOs span a broad range in accretion rate (see e.g., Merloni & Heinz 2008), and, therefore, of intrinsic luminosities. Deep X-ray surveys with *Chandra* and *XMM-Newton* have proven to be very efficient in revealing obscured accretion (except for Compton thick AGNs) down to relatively low luminosities (see Brandt & Hasinger 2005 for a review). According to the most recent synthesis models for the X-ray background (e.g., Gilli et al. 2007), the obscured AGN population (including heavily obscured Compton thick AGNs) outnumbers the unobscured one by a luminosity dependent factor ranging from ~ 2 at $L_X \simeq 10^{45}$ erg s^{-1} to ~ 8 at

$L_X \simeq 10^{42}$ erg s^{-1}. The evidence for a decreasing obscured AGN fraction toward high luminosities is supported by many other investigations (e.g., Ueda et al. 2003; Treister & Urry 2005), while there is increasing evidence that the fraction of obscured AGNs grows also toward high redshifts (La Franca et al. 2005; Treister & Urry 2006; Hasinger 2008).

By combining deep and shallow X-ray surveys (Ueda et al. 2003; La Franca et al. 2005; Hasinger et al. 2005; Silverman et al. 2008) it has been possible to address the issue of the X-ray LF evolution at high redshifts. Previous works presented tantalizing evidence for a decline of the comoving space density of X-ray selected AGNs at $z > 3$ in both the soft (0.5–2 keV; Hasinger et al. 2005; Silverman et al. 2005) and hard (2–10 keV; Silverman et al. 2008) bands, with a rate similar to that observed for optically selected quasars. At face value, these findings would imply that the space density of obscured AGNs, which are likely to be missed by optical surveys, declines toward high redshifts ($z > 3$) with a behavior similar to that of the unobscured AGNs, at least at the relatively high luminosities probed by present X-ray surveys ($\log L_X \gtrsim 44$). However, the results available so far are based on rather heterogeneous and relatively small samples, also affected by a significant level of spectroscopic incompleteness due to the faint magnitudes of the optical counterparts. To cope with this limitation, several photometric selection techniques have been proposed in recent years. Though differing in the details, the selection criteria for high-redshift, obscured AGNs are mainly based on a suitable combination of X-ray, optical and infrared flux ratios (see e.g., Fontanot et al. 2007). More specifically, hard X-ray emission associated with extremely faint or even undetected optical counterparts and extremely red colors (from optical up to mid-infrared wavelengths) is considered a reliable proxy for a high-redshift obscured AGNs (see e.g., Koekemoer et al. 2004; Brusa et al. 2005; Fiore et al. 2008). As an example, at the X-ray fluxes probed by the COSMOS survey, an X-ray to optical flux ratio $f_X/f_{\rm opt} > 10$ efficiently selects high z, Compton thin obscured AGN (see Fiore et al. 2003). Most of them have red or extremely red ($R - K > 5$) optical to near-infrared colors and indeed $f_X/f_{\rm opt}$ and $R - K$ are tightly correlated among X-ray selected sources (Brusa et al. 2005). Unfortunately, due to the widely different selection criteria, it is difficult to combine all the different approaches in order to obtain a reliable estimate of the space density of high-redshift obscured AGNs. Given the importance of the AGN LF at high redshift for our understanding of SMBH growth and evolution, the search for and the census of high-redshift ($z > 3$) AGNs warrant further efforts. The excellent multiwavelength coverage of the COSMOS field (Scoville et al. 2007) offers the unique opportunity to assemble the first statistically large, homogeneous, and well defined sample of X-ray-selected, high-redshift AGNs, which is almost completely unbiased against obscuration up to column densities of the order of $N_H \simeq 10^{23}$ cm^{-2}.

The paper is structured as follows. In Section 2 we describe the sample selection which is mainly based on the optical and multiwavelength identification of the *XMM*–COSMOS survey (Hasinger et al. 2007; Cappelluti et al. 2007; N. Cappelluti et al. 2009, in preparation; Brusa et al. 2007; M. Brusa, et al. 2009, in preparation), complemented by *Chandra* positions when available (M. Elvis et al. 2009, in preparation; S. Puccetti et al. 2009, in preparation; F. Civano et al. 2009, in preparation) to secure the correct optical counterpart, and, most importantly, by spectroscopic (Trump et al. 2009; Lilly et al. 2007) and high-quality photometric redshifts (Salvato et al. 2009). The optical and X-ray properties are presented in Sections 3 and 4, respectively. In Section 5 the number counts and space density of the sample are discussed and compared with model predictions. The results are summarized in Section 6, where the perspectives for future observations are also briefly outlined. A $H_0 = 70$ km s^{-1} Mpc^{-1}, $\Omega_M = 0.3$ and $\Omega_\Lambda = 0.7$ cosmology is adopted. Optical magnitudes are in the AB system.

2. THE SAMPLE

2.1. Parent sample

The Cosmic Evolution Survey (COSMOS) field (Scoville et al. 2007) is a so-far unique area with deep and wide multiwavelength coverage, from the optical band (*Hubble*, *Subaru* and other ground-based telescopes), to the infrared (*Spitzer*), X-rays (*XMM-Newton* and *Chandra*), and radio (Very Large Array (VLA)). The spectroscopic coverage with VIMOS/VLT and IMACS/Magellan, coupled with the reliable photometric redshifts derived from multiband fitting, is designed to be directly comparable, at $0.5 < z < 1.0$, to the 2dFGRS (Colless et al. 2001) at $z \sim 0.1$, and to probe the correlated evolution of galaxies, star formation, AGNs, and dark matter with large-scale structure in the redshift range $z \sim 0.5$–4.

The COSMOS field has been observed with *XMM-Newton* for a total of $\sim$ 1.5 Ms at a rather homogeneous depth of $\sim$ 50 ks (Hasinger et al. 2007; Cappelluti et al. 2007; N. Cappelluti et al. 2009, in preparation). The catalog used in this work includes 1848 pointlike sources[12] above a given threshold with a maximum likelihood detection algorithm in at least one of the soft (0.5–2 keV), hard (2–10 keV) or ultra-hard (5–10 keV) bands down to limiting fluxes of $\sim 5 \times 10^{-16}$, $\sim 3 \times 10^{-15}$ and $\sim 5 \times 10^{-15}$ erg cm^{-2} s^{-1}, respectively (see Cappelluti et al. 2007; N. Cappelluti et al. 2009, in preparation, for more details). The adopted likelihood threshold corresponds to a probability of $\sim 4.5 \times 10^{-5}$ that a catalog source is a spurious background fluctuation. Following M. Brusa et al. (2009, in preparation), we further excluded from this catalog 24 sources which turned out to be a blend of two *Chandra* sources and an additional 26 faint *XMM* sources coincident with diffuse emission (Finoguenov et al. 2007; A. Finoguenov et al. 2009, in preparation). To maximize the completeness over a well defined large area and, at the same time, keep selection effects under control, we considered only sources detected above the limiting fluxes corresponding to a coverage of more than 1 deg^2 in at least one of the three X-ray energy ranges considered, namely: 1×10^{-15} erg cm^{-2} s^{-1}, 6×10^{-15} erg cm^{-2} s^{-1}, and 1×10^{-14} erg cm^{-2} s^{-1}, in the 0.5–2 keV, 2–10 keV or 5–10 keV bands, respectively (N. Cappelluti et al. 2009, in preparation). The final sample includes therefore 1651 X-ray sources. The combination of area and depth is similar to that of the sample studied by Silverman et al. (2008, see their Figure 8). The main difference is given by the considerably higher redshift completeness of the parent sample obtained thanks to the much deeper coverage in the optical and near-IR bands and the systematic use of photometric redshifts (see below).

A detailed X-ray to optical association has been performed (M. Brusa et al. 2009, in preparation), applying the likelihood ratio technique on the optical, near-infrared (K-band) and mid-

[12] In the present analysis we used 53 out of the 55 *XMM* fields available; for this reason the number of sources is slightly lower than that discussed in N. Cappelluti et al. (2009, in preparation).

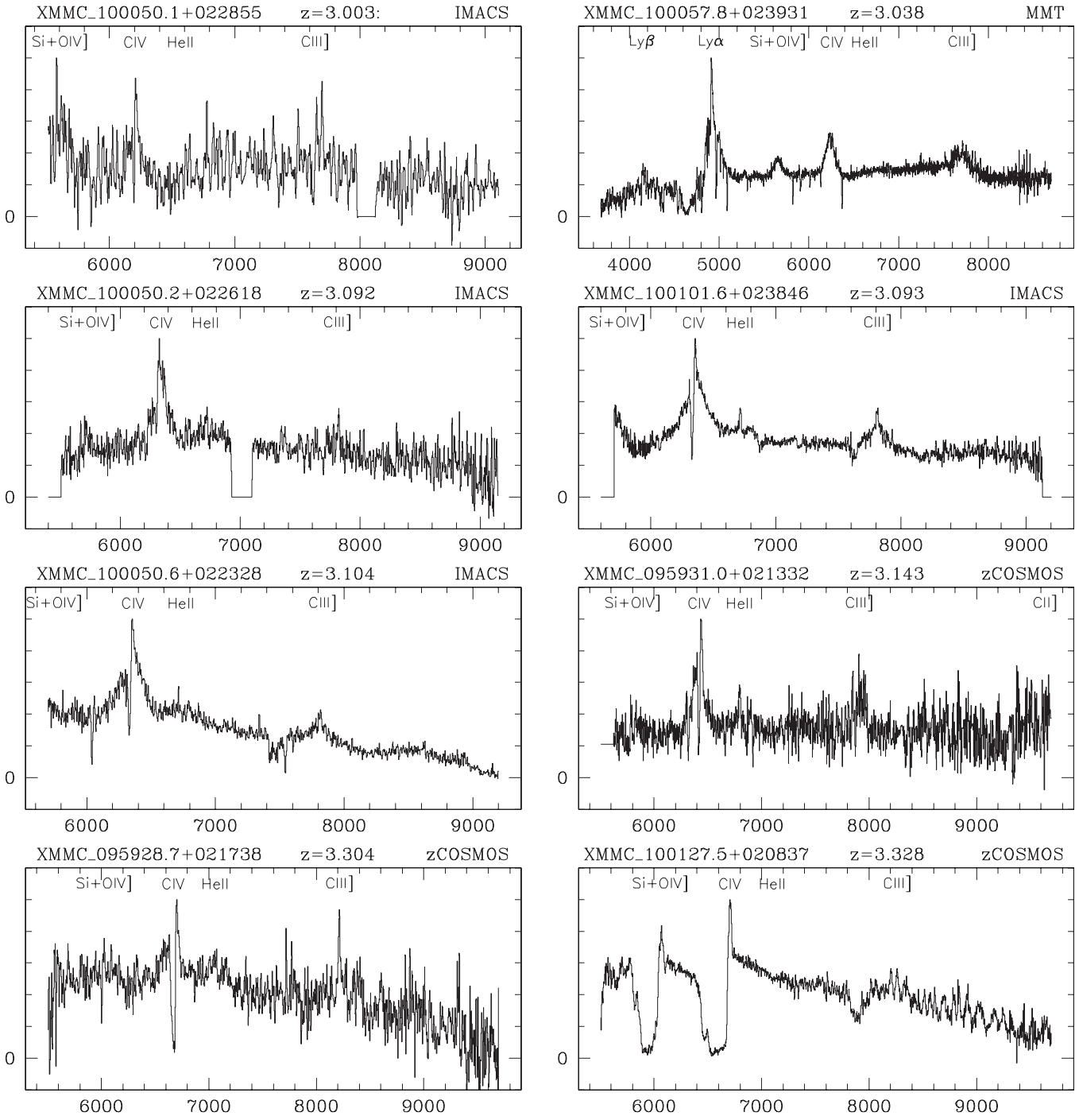

Figure 1. Spectra of the 22 spectroscopically confirmed $z > 3$ quasars, in order of increasing redshift. The spectra are shown in the observed frame and the main emission and absorption features are labeled. The three objects with single line spectra are marked with a ":" to the right of the redshift. The source of the spectra (IMACS, zCOSMOS or MMT is reported in the top right of each panel).

infrared (IRAC) catalogs available. In addition, for the subsample of ($\sim$ 50%) covered by *Chandra* observations, the ACIS images have been visually inspected to further exclude possible misidentification problems. Of the 1651 sources in the *XMM*–COSMOS catalog described above, 1465 sources have a unique/secure optical counterpart from the multiwavelength analysis, i.e., among them we expect only $\sim$ 1% of possible misidentifications (see discussion in M. Brusa et al. 2009, in preparation). For additional 175 sources, the proposed optical counterpart has about 50% probability to be the correct one. Given that the alternative counterparts of these 175 sources show optical to IR properties and redshift distribution comparable to the primary ones, the proposed ones can be considered statistically representative of the true counterparts of the X-ray sources. Therefore we consider also those in our analysis. Finally, 11 sources remain unidentified, because it was not possible to assign them to any optical and/or infrared counterpart.

Spectroscopic redshifts for the proposed counterparts are available from the Magellan/IMACS and MMT observation campaigns ($\sim$ 590 objects, Trump et al. 2007; Trump et al. 2009), from the zCOSMOS project ($\sim$ 350 objects; Lilly et al. 2007), or were already present either in the SDSS survey

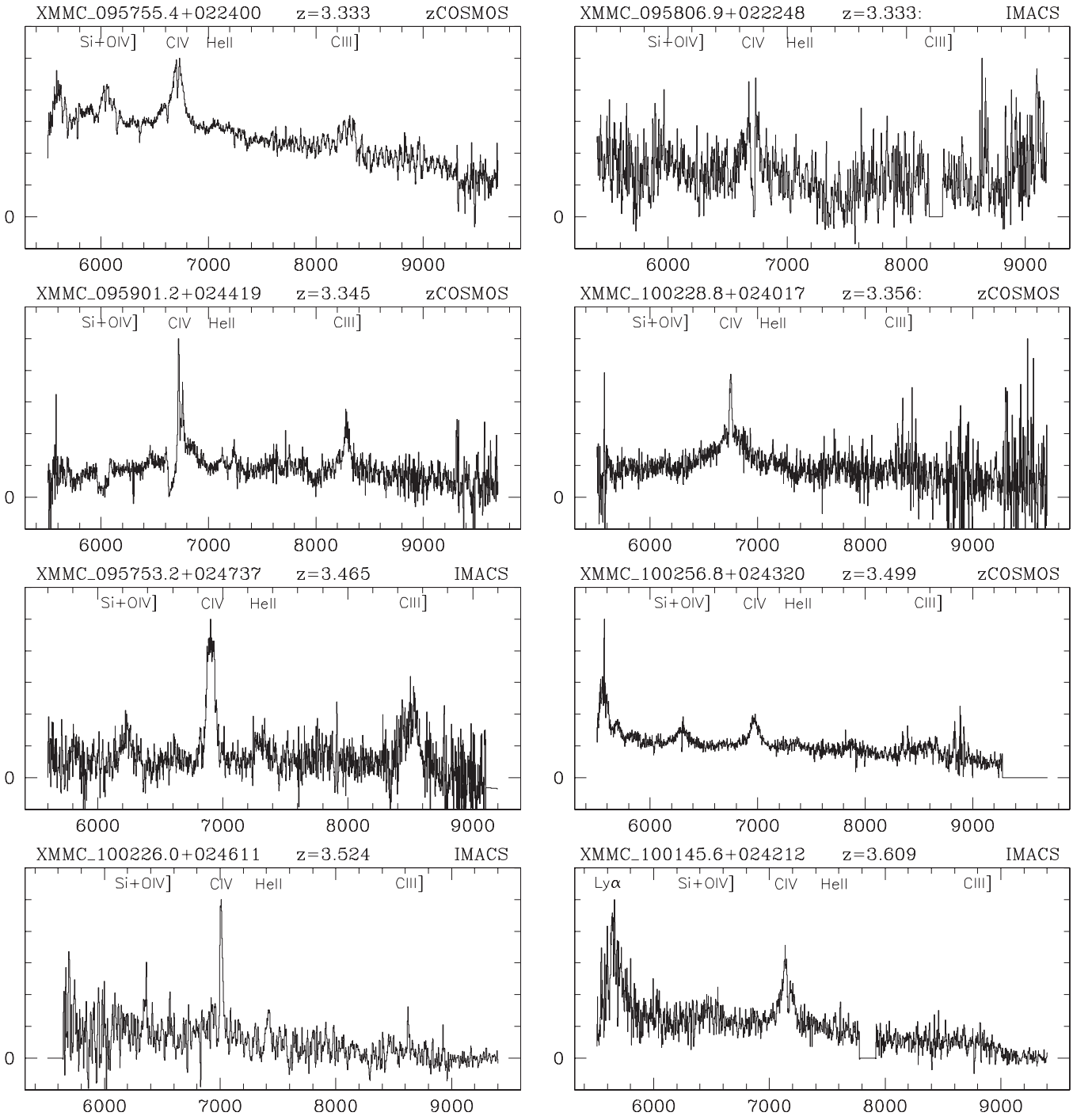

Figure 1. (Continued)

catalog (∼ 100 objects; Adelman-McCarthy et al. 2005; Kauffman et al. 2003[13]), or in the literature (∼ 95 objects, Prescott et al. 2006). In summary a total of 683 independent, good quality spectroscopic redshifts are available corresponding to a substantial fraction (∼ 40%) of the entire sample.

Photometric redshifts for all the *XMM*–COSMOS sources have been obtained exploiting the COSMOS multiwavelength database and are presented in Salvato et al. (2009). Since the large majority of the *XMM*–COSMOS sources are AGN, in addition to the standard photometric redshift treatments for normal galaxies, a new set of spectral energy distribution (SED) templates has been adopted, together with a correction for long-term variability and luminosity priors for pointlike sources (see Salvato et al. 2009 for further details). The availability of the intermediate-band *Subaru* filters (Y. Taniguchi et al. 2009, in preparation) is crucial in picking up emission lines (see also Wolf et al. 2004). This led, for the first time for an AGN sample, to a photometric redshift accuracy comparable to that achieved for inactive galaxies ($\sigma_{\Delta z/(1+z)} \sim 0.015$ and ∼ 5% outliers) at $i \lesssim 22.5$. At fainter magnitudes ($22.5 < I < 24.5$) the

[13] These sources have been retrieved from the NED, NASA Extragalactic Database and from the SDSS archive.

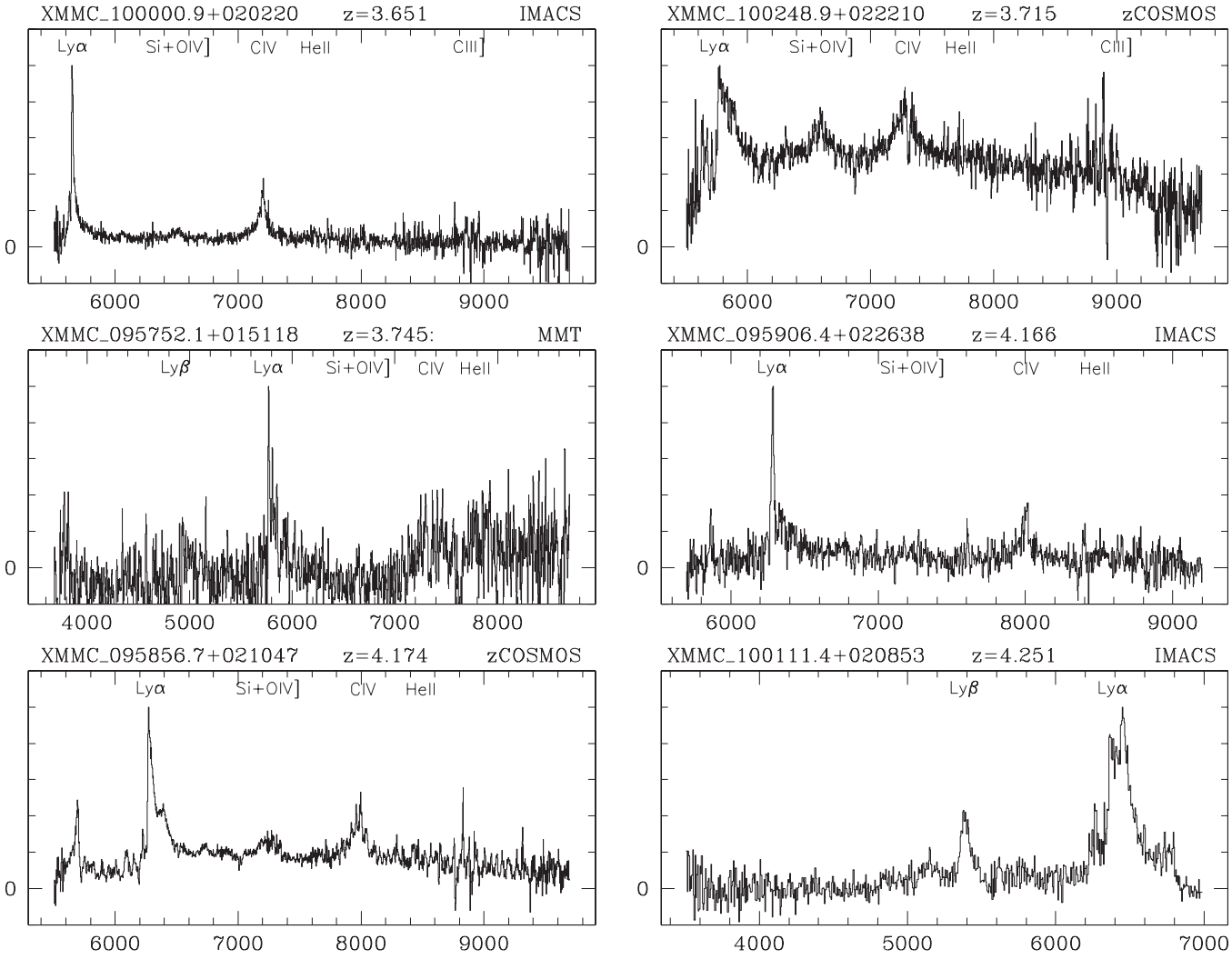

Figure 1. (Continued)

dispersion increases to $\sigma_{\Delta z/(1+z)} \simeq 0.035$ with $\sim 15\%$ outliers, still remarkably good for an AGN sample.

A photometric redshift is available for all but 36 objects out of 1651 in the flux-limited sample. Fourteen of them do not have multiband photometry, being detected only in the IRAC and *K* bands. The remaining 22 objects are affected by severe blending problems making the photo-*z* estimate unreliable.

2.2. The $z > 3$ QSO sample

We used the combined spectroscopic and photometric redshifts information available for our *XMM*–COSMOS sample to select $z > 3$ quasars. There are 40 *XMM*–COSMOS sources which have a spectroscopic (22) or photometric (18) redshifts larger than $z > 3$. Nineteen of them are detected in both the soft and hard bands, 20 are detected only in the soft band at fluxes larger than 1×10^{-15} erg cm^{-2} s^{-1} and one object is detected only in the hard band above the chosen threshold of 6×10^{-15} erg cm^{-2} s^{-1}, while it is just below the adopted limiting flux in the soft band.

Table 1 lists the names of the objects (following the standard IAU notation), the X-ray identifier number from the *XMM*–COSMOS catalog (N. Cappelluti et al. 2009, in preparation) used as reference identifier in the following, the identifier number from the COSMOS photometric catalog (Capak et al. 2007), the coordinates of the optical counterparts, and the basic properties of the sample (photometric and spectroscopic redshifts, *I*-band magnitude, X-ray fluxes and luminosities, and hardness ratio (HR)). The optical photometry used to derive the photometric redshifts can be retrieved by the public COSMOS photometric catalog available at IRSA[14] via the optical identifier number provided in the third column of Table 1. The deep *Chandra* survey in the COSMOS field covers about 0.9 deg^2 in the central region. *Chandra* images are available for about half (19) of the high-*z* QSOs in our sample and for these objects the identification of the counterparts is secure, thanks to the positional accuracy provided by *Chandra* spatial resolution. Following the discussion in M. Brusa et al. (2009, in preparation), we expect that, among the 21 sources without *Chandra* coverage, at most one can be a misidentification.

Spectroscopic redshifts are available for 22 sources, and are reported in Table 1. The observed frame spectra, sorted in order of ascending redshift, are shown in Figure 1, with all the major emission lines labeled. For four of them, the spectroscopic redshift is based on a single, broad line identified as CIV1549 or Lyα. In all four cases, the photometric redshift rules out

[14] http://irsa.ipac.caltech.edu/data/COSMOS/tables/cosmos_phot_20060103.tbl.gz

Table 1
Coordinates and Properties of the $z > 3$ QSOs from the *XMM*–COSMOS Sample

IAU Name[a]	XID[b]	ID[c]	R.A.[d] hh:mm:ss	Decl.[d] dd:mm:ss	zspec	zphot	i (AB)	$F_{0.5-2\,\mathrm{keV}}$ 10^{-15} cgs	$\log L_{2-0\,\mathrm{keV}}$[h] cgs	HR
XMMC_J100101.6+023846	326	2668917	10:01:01.51	+02:38:48.68	3.003[g]	3.06 (3.04–3.08)	23.23	1.21	44.05	< -0.53
XMMC_J100157.5+014446	2518	448852	10:01:57.72	+01:44:47.05	...	3.01 (2.96–3.06)[e]	23.96	1.31	44.26	0.17
XMMC_J100119.9+023444	418	2289051	10:01:20.05	+02:34:43.82	...	3.03 (1.58–3.84)[f,i]	27.02	1.73	44.25	−0.28
XMMC_J100226.0+024611	5331	2558690	10:02:26.11	+02:46:10.78	3.038	3.04 (3.02–3.06)	20.28	4.58	44.62	−0.59
XMMC_J100223.2+022557	10690	1849901	10:02:23.31	+02:25:58.17	...	3.09 (3.06–3.12)	23.24	1.29	44.10	< -0.40
XMMC_J100050.6+022328	349	1977373	10:00:50.58	+02:23:29.30	3.092	3.09 (3.06–3.10)	22.58	1.76	44.29	−0.23
XMMC_J095755.4+022400	2407	2132709	09:57:55.47	+02:24:01.18	3.093	0.99 (0.96–1.02)	21.26	11.4	45.06	−0.46
XMMC_J095931.8+023018	262	2421306	09:59:31.80	+02:30:18.51	...	3.10 (2.46–3.26)[e,i]	25.82	5.69	44.75	−0.50
XMMC_J095806.9+022248	2421	2137194	09:58:06.98	+02:22:48.59	3.104	3.11 (3.08–3.12)	20.89	5.22	44.73	−0.41
XMMC_J095840.6+021003	5347	1749560	09:58:40.71	+02:10:03.72	...	3.13 (2.60–3.24)[f]	24.71	2.05	44.29	< -0.57
XMMC_J095859.5+024356	5161	2768843	09:58:59.70	+02:43:55.25	...	3.14 (3.10–3.18)	24.00	1.64	44.29	−0.14
XMMC_J100228.8+024017	5175	2583306	10:02:28.82	+02:40:17.08	3.143	3.13 (3.10–3.16)	22.07	6.63	44.84	−0.44
XMMC_J100220.3+020452	5345	1131048	10:02:20.37	+02:04:52.91	...	3.29 (3.26–3.32)	23.15	1.86	44.31	< -0.50
XMMC_J100023.4+020115	469	1259457	10:00:23.24	+02:01:17.40	...	3.30 (3.14–3.40)	24.42	1.08	44.10	< -0.40
XMMC_J100256.8+024320	5219	2534376	10:02:56.92	+02:43:21.27	3.304	3.25 (3.22–3.28)	22.25	2.21	44.39	< -0.42
XMMC_J095740.6+025259	60311	3190185	09:57:40.70	+02:52:58.77	...	3.31 (3.28–3.34)	21.92	2.99	44.51	< -0.11
XMMC_J100113.3+014542	53733	485583	10:01:13.45	+01:45:41.89	...	3.32 (3.26–3.40)	25.02	1.00	44.07	< -0.44
XMMC_J100111.4+020853	60131	1593500	10:01:11.34	+02:08:55.84	3.328[d]	3.47 (3.44–3.50)	20.53	1.09	44.21	0.10
XMMC_J100050.1+022855	180	2350265	10:00:50.12	+02:28:54.97	3.333	3.34 (3.32–3.36)	20.17	2.96	44.51	< -0.73
XMMC_J100127.5+020837	2394	1594618	10:01:27.53	+02:08:37.79	3.333[g]	3.31 (3.28–3.34)	23.16	3.37	44.61	−0.36
XMMC_J095928.7+021738	1151	2039436	09:59:28.72	+02:17:38.57	3.345[d]	3.38 (3.36–3.40)	21.77	3.41	44.67	−0.08
XMMC_J100057.8+023931	187	2665989	10:00:57.79	+02:39:32.61	3.356[c]	3.33 (3.30–3.36)	22.36	3.78	44.67	−0.38

Table 1
(Continued)

IAU Name[a]	XID[b]	ID[c]	R.A.[d] hh:mm:ss	Decl.[d] dd:mm:ss	zspec	zphot	i (AB)	$F_{0.5-2keV}$ 10^{-15} cgs	$\log L_{2-0keV}$[h] cgs	HR
XMMC_J095923.0+022853	5482	2426654	09:59:22.98	+02:28:54.03	...	3.36 (3.34–3.38)	23.22	1.70	44.34	−0.26
XMMC_J100255.6+013057	60186	46132	10:02:55.81	+01:30:58.05	...	3.40 (0.22–3.42) [f]	22.11	2.98	44.54	< −0.08
XMMC_J100145.6+024212	5382	2615665	10:01:45.58	+02:42:12.59	3.465	3.44 (3.42–3.46)	23.08	1.14	44.17	< −0.31
XMMC_J100256.6+021159	5116	1462117	10:02:56.53	+02:11:58.48	...	3.47 (3.46–3.50)	20.29	4.15	44.73	−0.43
XMMC_J100000.9+020220	5583	1294973	10:00:01.05	+02:02:20.03	3.499	3.49 (3.48–3.52)	21.88	1.48	44.28	< −0.57
XMMC_J095901.2+024419	5162	2767217	09:59:01.29	+02:44:18.81	3.524[e,m]	3.52 (3.50–3.56)	22.93	1.92	44.45	−0.11
XMMC_J100312.0+024916	53351	2910750	10:03:12.06	+02:49:15.75	...	3.53 (2.22–3.70) [f,i]	24.86	2.84	44.63	−0.04
XMMC_J095753.2+024737	5199	3176366	09:57:53.49	+02:47:36.25	3.609	3.61 (3.58–3.62)	21.96	2.68	44.60	−0.21
XMMC_J095854.2+023753	5525	2832144	09:58:54.36	+02:37:53.38	...	3.65 (3.62–3.66)	22.28	2.82	44.64	−0.13
XMMC_J100232.9+022331	60007	1859446	10:02:33.23	+02:23:28.86	...	3.65 (3.62–3.68)	22.17	0.96[l]	44.21	0.14
XMMC_J095931.0+021332	504	1694357	09:59:31.01	+02:13:33.01	3.651	3.65 (3.62–3.66)	22.72	1.48	44.32	< −0.53
XMMC_J100104.2+014202	2602	500928	10:01:04.17	+01:42:03.13	...	3.70 (1.42–4.04)[f]	24.79	1.87	44.44	< −0.62
XMMC_J100050.2+022618	300	1965822	10:00:50.16	+02:26:18.48	3.715	3.54 (3.52–3.56)	21.24	1.62	44.38	< −0.57
XMMC_J100248.9+022210	5592	1864254	10:02:48.90	+02:22:12.07	3.745[g]	3.76 (3.74–3.80)	22.47	2.21	44.52	< −0.41
XMMC_J095906.4+022638	5606	2042408	09:59:06.46	+02:26:39.50	4.166[e,m]	4.01 (3.96–4.06)	22.79	1.33	44.42	< −0.51
XMMC_J095752.1+015118	5594	1061300	09:57:52.16	+01:51:20.15	4.174	3.73 (3.70–3.74)	21.08	1.27	44.40	< −0.28
XMMC_J095856.7+021047	54439	1705273	09:58:56.69	+02:10:47.75	4.241[i]	4.24 (4.22–4.26)	23.53	1.36	44.45	< −0.37
XMMC_J100152.0+023152	5259	2260872	10:01:52.10	+02:31:55.19	...	4.45 (4.42–4.50)[i]	26.36	1.08	44.39	< −0.49

Notes.

[a] Official IAU designation for the *XMM*–COSMOS sources.

[b] X-ray identifier number from the *XMM*–COSMOS catalog (N. Cappelluti et al. 2009, in preparation).

[c] Optical identifier number from the photometric COSMOS catalog published by Capak et al.(2007). Photometry in the optical bands can be retrieved from IRSA at the link: http://irsa.ipac.caltech.edu/data/COSMOS/tables/cosmos_phot_20060103.tbl.gz.

[d] Coordinates of the optical counterpart of the X-ray source.

[h] Rest-frame hard X-ray luminosity.

[e] Objects with large χ^2 minima (extending at $z < 3$).

[f] Objects which have a comparable photo-z solution at $z < 3$.

[g] Single line spectrum.

[d] BAL QSO.

[i] Undetected in the U-band.

[l] Source detected in the hard band, but below the threshold (10^{-15} erg cm^{-2} s^{-1}) in the soft band.

[m] Candidate NL QSO (FWHM < 1500 km s^{-1}).

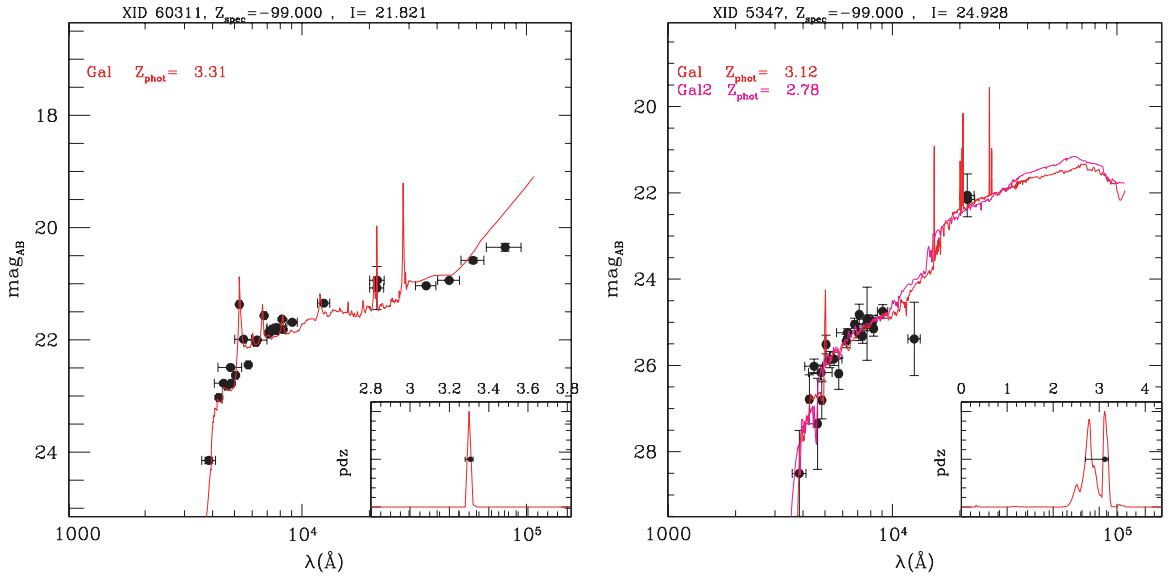

Figure 2. Two examples of photometric redshift determination for sources without a spectroscopic redshift: a photo-z with a unique solution (XID 60311) and an object with two possible solutions for the photometric redshift (XID 5347). Black points are the observed photometry from the U-band to IRAC 8.0 μm. The red curve is the best fit template. The inset in the bottom right shows the probability distribution function (PDS; normalized to one) as a function of redshift.

(A color version of this figure is available in the online journal.)

alternative solutions at lower redshift, favoring the proposed $z > 3$ nature.

In all but two cases there is convincing evidence for the presence of broad optical lines. For two sources (XID 5162 and XID 5606) the most prominent emission lines are narrow (FWHM$<$ 1500 km s^{-1}), making these objects Type 2 QSO candidates.

For the remaining 18 sources, only photometric redshifts are available. The photometric redshifts for the entire $z > 3$ sample, with associated errors (1σ) are reported in Table 1. A detailed discussion on the quality and reliability of AGN photometric redshifts is presented elsewhere (Salvato et al. 2009). Here we just note that all but one (XID 2407) of the objects with spectroscopic redshifts have photometric redshifts well consistent with the spectroscopic ones, with 60% of the spectroscopic redshifts being within the 1σ range of the photometric ones. Also the fraction of outliers (1 source out of 22) is consistent with the expectations for the entire photo-z catalog (5%, see Section 2.1). However, we should also note that spectroscopic redshifts are available for the brightest (i $\lesssim$ 23) sample and a higher fraction of outliers (up to 15%) is expected at fainter optical magnitudes.

Salvato et al. (2009) also computed PDFs for the photometric redshift solutions. In the sample of 40 quasars, five objects have the first solution (i.e., the highest value of PDF) at $z > 3$, but also a comparable solution (in terms of PDF) at $z < 3$. Most of these objects have $i \gtrsim 24$. Conversely, there are additional 14 objects in the entire sample of *XMM*–COSMOS counterparts with a first solution at $z < 3$, but a second solution at $z > 3$. Figure 2 shows two examples of the SED fitting and photometric redshift determination, one for a source with single solution (XID 60311, left panel) and one for an object with multiple, secondary solutions at lower redshift (XID 5347, right panel). Weighting the objects with their PDFs, we obtain that $\sim$ 60% of the 32 objects without spectroscopic redshifts and with either unique, first or second solution at $z > 3$ are expected to be at $z > 3$. This translates to $\sim$ 20 objects, close to the 18 objects with primary solution at $z > 3$, which are listed in Table 1.

Among the 22 sources lacking a photometric redshift, due to problems related to blends or saturation, six have spectroscopic redshifts which place them at $z < 1.5$. We expect that the redshift distribution of these sources follows that of the total sample, with only 3% (22/683, e.g., $\sim$ 1 object) being at $z > 3$. It should also be noted that the 14 objects undetected in the optical bands (10 of them detected in the soft band above the adopted limiting flux) and without an estimate of the photometric redshift, are candidate high-redshift, possible obscured QSOs (see e.g., Koekemoer et al. 2004; Mignoli et al. 2004).

Summarizing, we conclude that, although the fraction of objects in our sample which have only a photometric redshift is close to 50%, the total number of objects with $z > 3$ is statistically robust. Even if some of the 18 objects without spectroscopic redshift are likely to be at $z < 3$, this number is expected to be almost exactly compensated by the number of objects which, being at $z > 3$, have instead their best photometric solution at $z < 3$. Therefore, we consider the 40 objects listed in Table 1 as representative of the real number of sources at $z > 3$. We will quantify in Section 6 the possible contribution of objects undetected in the optical bands to the total number of $z > 3$ QSOs.

Figure 3 shows the magnitude distribution of the $z > 3$ sample (blue filled histogram) compared with the overall optical population (black open histogram). The median magnitude of the $z > 3$ sample ($i = 22.72$, with a dispersion of 1.02 mag) is about 0.8 magnitudes fainter than that of the overall *XMM*–COSMOS population ($i = 21.90$, with a dispersion of 1.32). Spectroscopically confirmed $z > 3$ objects (green histogram in the figure) are in the bright tail of the magnitude distribution of the high-redshift sample. A non-negligible fraction of the objects in the sample (7/40) has $i > 24.5$ and, as pointed out above, a somewhat more uncertain photo-z solution (see Table 1).

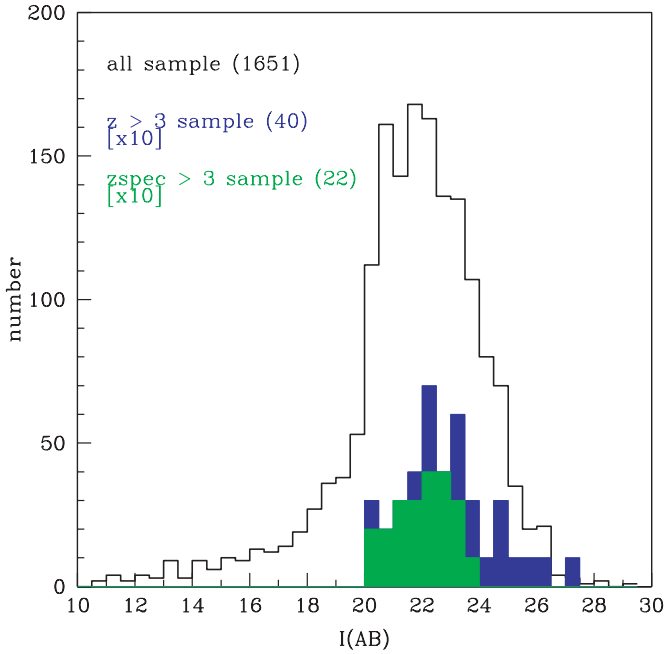

Figure 3. Histogram of the *i*-band magnitude distribution for the global *XMM*–COSMOS sample (empty), the $z > 3$ sample (blue) and the spectroscopic $z > 3$ sample (green).

(A color version of this figure is available in the online journal.)

3. OPTICAL COLORS

Multiband optical photometry provides a routinely-adopted, reliable selection technique to select high-redshift QSOs. The method was first applied to AGNs in the 1960s, based on the inference that quasars often have a larger ultraviolet excess than the hottest stars (Sandage & Wyndham 1965), and subsequently extended to large-scale surveys (e.g., Schmidt & Green 1983, Croom et al. 2001, Fan et al. 2001, Richards et al. 2006). The most suitable combination of colors strongly depends on the redshift range. For example, the "UV excess" technique is optimal for $z < 2.0$–2.2. At $z > 3$ an efficient selection method is known as Lyman Break technique and has been extensively used to select $z > 3$ QSOs and galaxies (see, e.g., Steidel et al. 1996; Hunt et al. 2004; Aird et al. 2008). Assuming a standard QSO template and including absorption by the intergalactic medium (IGM, i.e., the Lyman-α forest), it is possible to efficiently isolate $z > 3$ QSOs in the $U - g'$ versus $g' - r'$ color–color plane (i.e., Siana et al. 2008).

A somewhat different color–color plot ($v - i$ versus $B - v$) has been extensively discussed by Casey et al. (2008). The three photometric bands have been chosen in order to minimize the problems due to AGN variability: COSMOS observations in the B, v, and i bands were taken at the same epoch, providing almost simultaneous colors, while the g' and U band observations were taken about one year apart (Taniguchi et al. 2007, Capak et al. 2007). For efficient selection at $z > 3$ Casey et al. (2008) make a diagonal cut in the two colors diagram, described by the relation: $v - i < 1.15 \times (B - v) - 0.31$.

The X-ray-selected QSOs of our sample are plotted in the $v - i$ versus $B - v$ plane in Figure 4 (left panel) with associated errors. The 20 spectroscopically confirmed BL AGNs are marked with blue circles, while the two objects classified as NL AGNs are shown as red triangles. Eight objects ($\sim 20\%$) lie above the nominal line proposed by Casey et al. (2008) to select $z > 3$ QSOs in the COSMOS field. Among them two sources (XID 2407 and XID 5606) have a spectroscopic redshift. These objects would have not been selected as high-redshift quasars from this optical color–color diagram. We should note, however, that the Casey et al. (2008) criterion was tested for relatively bright ($i < 24.5$) sources with compact morphology defined in terms of Gini coefficient larger than ~ 0.8. If we further impose the same optical limit to the objects of our sample, and consider only the objects classified as pointlike from the attitude control

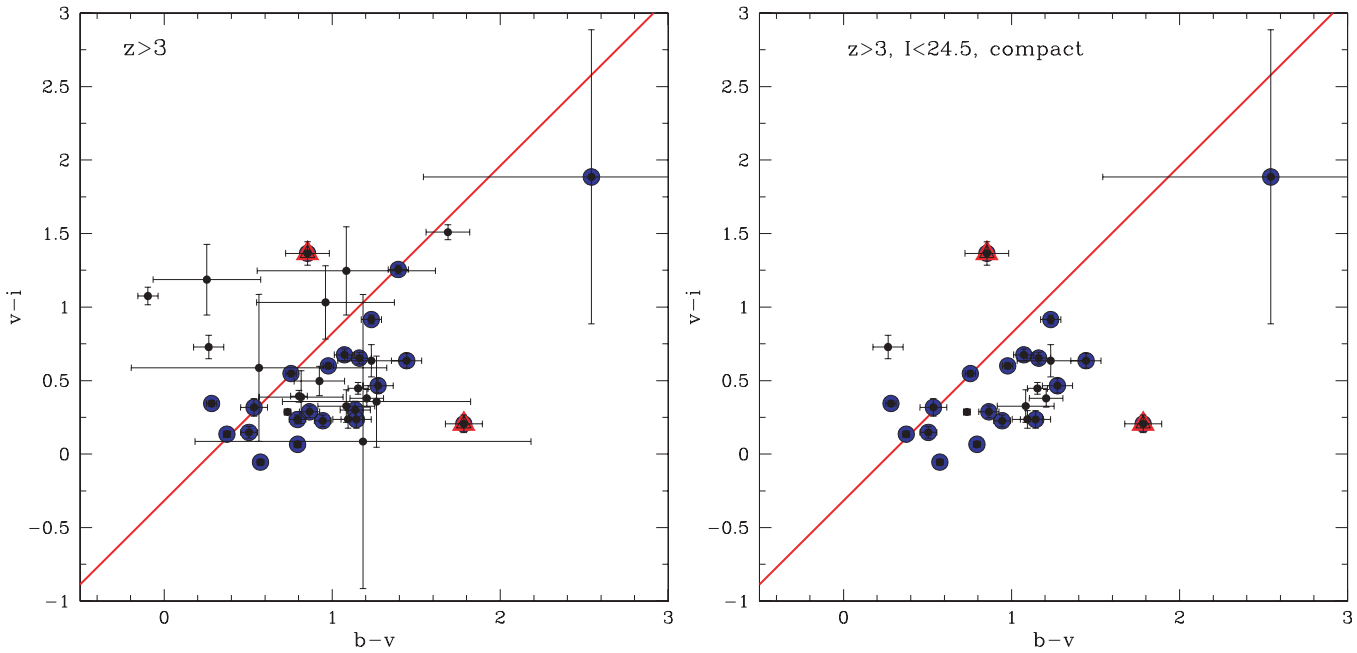

Figure 4. Left panel: $v - i$ vs. $B - v$ color–color diagram for the $z > 3$ sources. Black points correspond to all $z > 3$ sources, blue circles to the 20 objects classified as BL AGNs, red triangles refer to the two objects classified as NL AGNs. Outliers from the QSO locus are those on the left of the red solid line, defined as: $[v - i < 1.15 \times (B - v) - 0.31]$. Right panel: same as the previous panel, but only for the subsample with $i < 24.5$ and compact morphology.

(A color version of this figure is available in the online journal.)

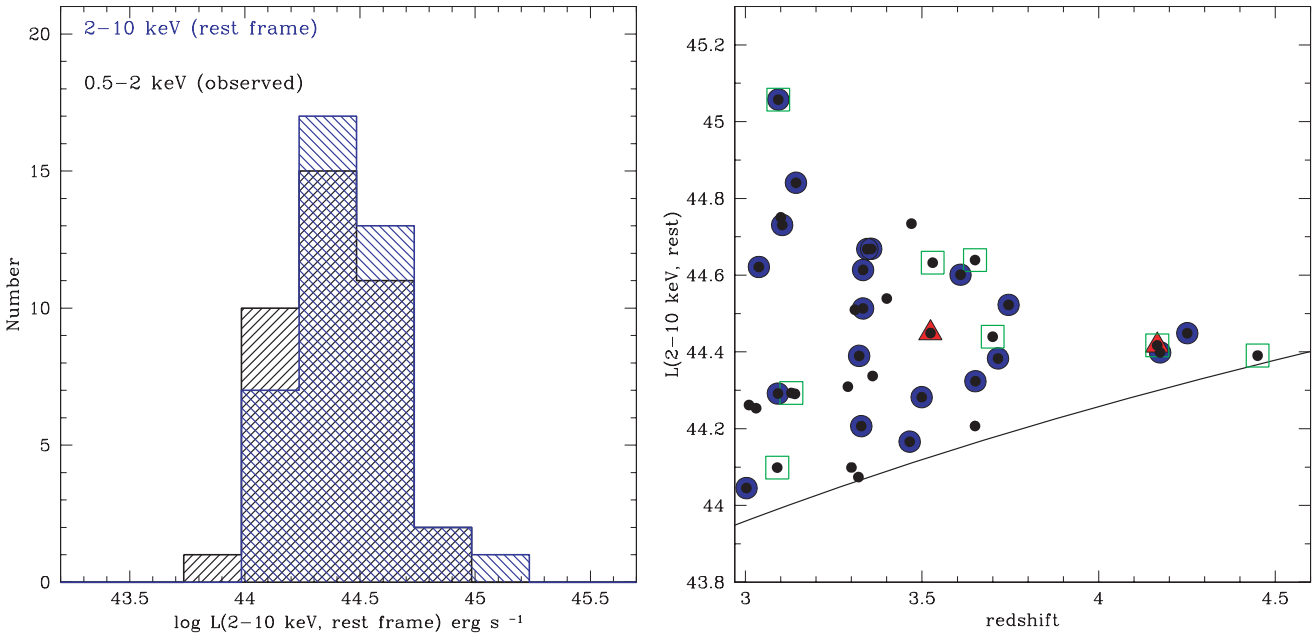

Figure 5. Left panel: histogram of the rest frame 2–10 keV luminosity calculated assuming the spectral slope derived from the ratio of the fluxes in the rest frame soft and hard bands (blue histogram, see the text for details) compared with the rest frame 2–10 keV luminosities calculated using the observed 0.5–2 keV fluxes (i.e., the rest frame 2–10 keV flux at $z > 3$, black histogram). Right panel: the luminosity–redshift plane for the objects in our sample. Symbols as in previous figures. Green squares mark the outliers from the optical color–color diagram of Figure 4. The continuous line represents the luminosity limit of the survey computed from the 0.5–2 keV limiting flux.

(A color version of this figure is available in the online journal.)

system (ACS) analysis (Leauthaud et al. 2007), only three out of 25 ($\sim$ 12%) lie above the dividing line (Figure 4, right panel). The eight objects above the dividing line in the left panel of Figure 4 are, therefore, on average, optically faint ($i > 24.5$) and/or with an extended morphology. These objects would not have been selected as high-redshift candidates by an optical survey. We name these objects "outliers" and investigate their average X-ray properties in the following. Conversely, if we consider the full sample of *XMM* sources with $i < 24.5$ and "compact" morphology, there is a total of 60 objects that lie below the diagonal line in Figure 4: 25 shown in the right panel of Figure 4 plus 35 additional objects. The majority of these 35 objects (25/35) has a good quality spectroscopic redshift lower than 3, and in most of the cases (20/25) they are classified as BL AGNs at $z \sim$ 1–3. As discussed by Casey et al. (2008) the contamination of low-redshift sources in this optical color–color diagram can be as high as 50%–70%.

4. X-RAY PROPERTIES

For each object with given redshift (either spectroscopic or photometric) the flux in the rest frame 2–10 keV band has been calculated, assuming the spectral slope derived from the ratio of the fluxes in the rest-frame hard and soft band.[15] Rest frame 2–10 keV fluxes have been then converted into luminosities within the adopted cosmology. Figure 5 (left panel) shows the histogram of the rest frame, 2–10 keV luminosities for the 40 sources in the present sample. The rest frame 2–10 keV luminosities calculated using the observed 0.5–2 keV fluxes (roughly corresponding to the rest frame 2–10 keV fluxes at $z \geqslant 3$) are consistent with those derived with the method described above (see black histogram in Figure 5). All the objects in the $z > 3$ sample have hard X-ray (2–10 keV) rest-frame luminosities in the interval 10^{44}–10^{45} erg s^{-1}. The luminosity–redshift plane in the redshift interval $z = 3.0$–4.5 is shown in Figure 5 (right panel). Sources with a spectroscopic redshift are plotted with blue (20 BL AGN) and red (2 NL AGN) symbols. The continuous line represents the luminosity limit of the survey computed from the 0.5–2 keV limiting flux.

The HR (defined as $(H - S)/(H + S)$, where H and S are the counts detected in the 2–10 keV and 0.5–2 keV bands, respectively) as a function of the redshift for all the 40 objects in our sample is shown in Figure 6. For the 20 sources detected only in the soft band, upper limits have been obtained by conservatively assuming 25 hard counts. Loci of constant N_H at different redshifts for a power law spectrum with $\Gamma = 1.7$ are also reported with dashed lines.[16] The shaded region marks the expected HR for an unabsorbed power-law with $\Gamma = 1.7$ (upper limit) and $\Gamma = 1.8$ (lower limit). The objects in our sample span a rather large range of HR and corresponding N_H values, from unobscured to column densities up to log $N_H \simeq 23.7$.

To increase the statistics and gain information on the average spectral properties of the different sources in the sample, we performed a stacking analysis of the source spectra. The spectra were extracted for all the sources in their rest frame 2–22 keV band from the EPIC *pn* data and corrected for the local background, following the procedure outlined in Mainieri et al. (2007). Three sources (XID 5259, 5592, and 5594), which have null or negative counts in this energy range when the local background is subtracted, are excluded from the analysis here. Two additional sources (60186 and 60311) which do not show stringent upper limits in the HR are further excluded. The individual spectra were then corrected for the instrumental

[15] Within each observed band the counts are converted into fluxes assuming $\Gamma = 2$ in the 0.5–2 keV and $\Gamma = 1.7$ in the 2–10 keV, as in Cappelluti et al. 2007.

[16] We did not consider a reflection component because it is not observed at the X-ray luminosities considered in this work.

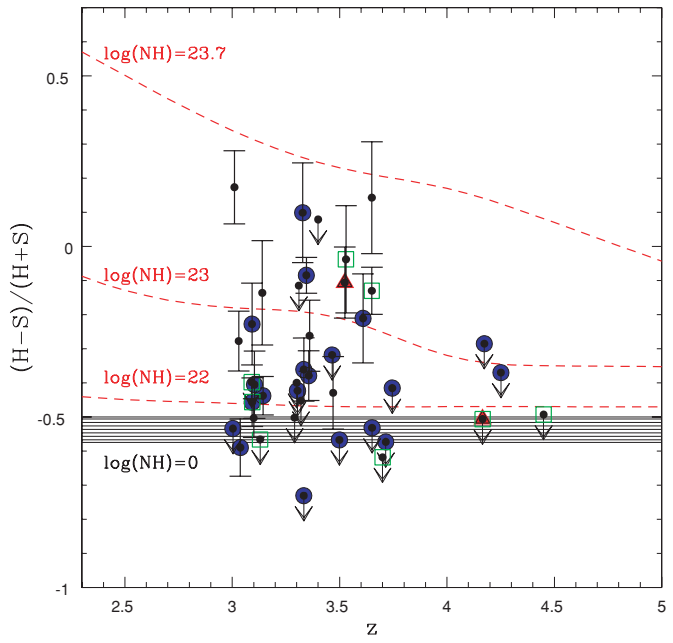

Figure 6. HR vs. redshift for the $z > 3$ QSOs sample (symbols as in previous figures). The dashed lines correspond to the loci of constant $N_{\rm H}$ for a power-law spectrum with $\Gamma = 1.7$. The shaded region marks the expected HR for an unabsorbed power law with $\Gamma = 1.8$ (lower limit) and $\Gamma = 1.7$ (upper limit).

(A color version of this figure is available in the online journal.)

Table 2
Summary of Stacking Results for the $z > 3$ QSOs Samples

Sample	No. of Sources	Total Net Counts	Γ Simple PL
$\log N_H < 23$	26	1200.9	$1.8^{+0.2}_{-0.3}$
$\log N_H > 23$	9	342.4	$0.9^{+0.7}_{-0.8}$
$\log N_H < 23$, BL AGN	16	782.1	$1.7^{+0.3}_{-0.3}$
$\log N_H < 23$, photo-z	10	418.8	$1.5^{+0.4}_{-0.5}$

response curve, brought to the rest-frame and stacked together with energy intervals of 1 keV. Noisy spectral channels of the stacked spectra were binned further, when appropriate.

First, we divided the sample into two subsamples based on the HR: the sources showing an indication of "soft" spectrum from the HR (i.e., the 26 objects below the locus of $N_{\rm H} = 10^{23}$ cm^{-2} at different redshifts) and the sources with an indication of a "hard" spectrum (i.e., the nine objects above the $N_{\rm H} = 10^{23}$ cm^{-2} locus). The stacked spectra for these two sub–samples are shown in Figure 7 and the results from a power-law fit are summarized in Table 2. The "soft" sources (open squares in Figure 7) have a steeper spectral slope ($\Gamma \sim 1.8 \pm 0.3$) than the "hard" sources (filled squares: $\Gamma \sim 0.9 \pm 0.8$), demonstrating that the HR analysis (which is based on the X-ray color in the observed frame) can isolate the most absorbed sources even at these high redshifts.

The fraction of log $N_{\rm H} \geqslant 23$ AGNs, computed weighting with the errors the number of sources with HR above the $\log N_{\rm H} = 23$, is $\sim$ 20%, somewhat larger than the Gilli et al. (2007) expectations[17] ($\sim$ 10%) for the same luminosity, redshifts and flux limits of our survey.

It is interesting to note that one of the two objects with narrow emission lines in the optical spectrum (XID 5162, $z = 3.524$) has an HR (~ -0.11, red triangle in Figure 6) consistent with a column density $\log N_H > 23$ and therefore would be classified as a Type 2 QSO from both the optical and the X-ray diagnostics. This object is one of the highest-redshift, radio-quiet, spectroscopically confirmed Type 2 QSOs (see e.g., Norman et al. 2002; Mainieri et al. 2005). The other two objects with $\log N_H > 23$ and spectroscopic redshift (XID 60131 at $z = 3.328$, and XID 1151 at $z = 3.345$) show clear signatures of broad absorption lines (BAL) in their optical spectra (Figure 1). Column densities of the order of $\log N_H \sim 23$ are common among those BAL QSOs for which good quality X-ray spectra are available (Gallagher et al. 2002). Significant X-ray absorption in BAL QSOs is detected up to $z \sim 3$ (Shemmer et al. 2005).

It is important to note, however, that the HR at $z > 3$ is not very sensitive to column densities below $\log N_{\rm H} \simeq 23$. Given also the typical dispersion in the intrinsic power-law spectra, it is possible that the subsample of "soft" sources contains also some of these absorbed AGN. These sources are expected to be optically faint (e.g., Alexander et al. 2001; Fiore et al. 2003; Mainieri et al. 2005; Cocchia et al. 2007) and thus among the still spectroscopically unidentified sources. In order to test this possibility, we further divided the "soft" sample into two subsamples: sources without a spectroscopic redshift available (10) and sources spectroscopically identified as BL AGN (16, see Figure 7, right panel). There is evidence of absorption (below $\sim$ 3 keV, corresponding to $\log N_{\rm H} \sim$22.5) in the average spectrum of spectroscopically unidentified sources. The X-ray counting statistics does not allow to establish, on a source by source basis, whether the "outliers" of optical color–color diagrams are also obscured in the X-rays. Given that the five "outliers" from the optical color–color diagram make up about 30% of this absorbed sample, it may well be possible that they are responsible of the low energy cut-off in the stacked spectrum (right panel of Figure 7).

5. EVOLUTION OF $Z > 3$ QSOs

5.1. Number Counts

We derived the log N–log S of the $z > 3$ *XMM*–COSMOS QSOs by folding the observed flux distribution with the sky coverage. The binned log N–log S relation of the 39 objects with a 0.5–2 keV flux larger than 10^{-15} erg cm^{-2} s^{-1} is plotted in Figure 8 (red points, with associated Poissonian errors). The green shaded area represents an estimate of the maximum and minimum number counts relation at $z > 3$ under somewhat extreme assumptions. The lower bound is obtained by considering only the 22 sources with a spectroscopic redshift,[18] while the upper bound includes in the $z > 3$ sample also the 10 objects with a 0.5–2 keV flux larger than 10^{-15} erg cm^{-2} s^{-1}and without a detection in the optical band, as well as the 11 objects above the same flux threshold and with a second photometric redshift solution at $z > 3$ (see Section 2). Under these assumptions, the lower limit corresponds to the (very unlikely) hypothesis that all the photometric redshifts are overestimated, while the upper limit corresponds to the assumption that non-detection in the optical band is a very reliable proxy of high

[17] The expectations have been computed using the Portable Multi Purpose Application for the AGN COUNTS (POMPA-COUNTS) software available online at: http://www.bo.astro.it/gilli/counts.html.

[18] We included also the three objects with a "single line" spectrum, given that the photometric redshift solution discarded alternative solutions at lower redshift.

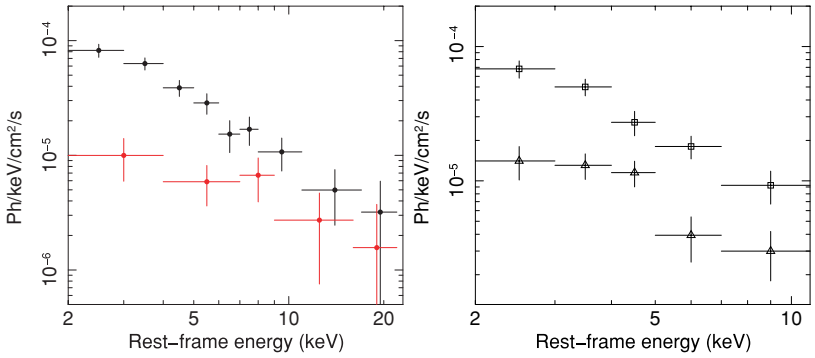

Figure 7. Left panel: rest-frame stacked spectra of sources with log NH $<$ 23 at all redshifts (26 objects, black circles) and with log NH $>$ 23 (9 objects, red circles). Right panel: rest-frame stacked spectra of the sources with log NH $<$ 23 further divided into BL AGNs (16 objects, squares) and spectroscopically unidentified sources (10 objects, triangles).

(A color version of this figure is available in the online journal.)

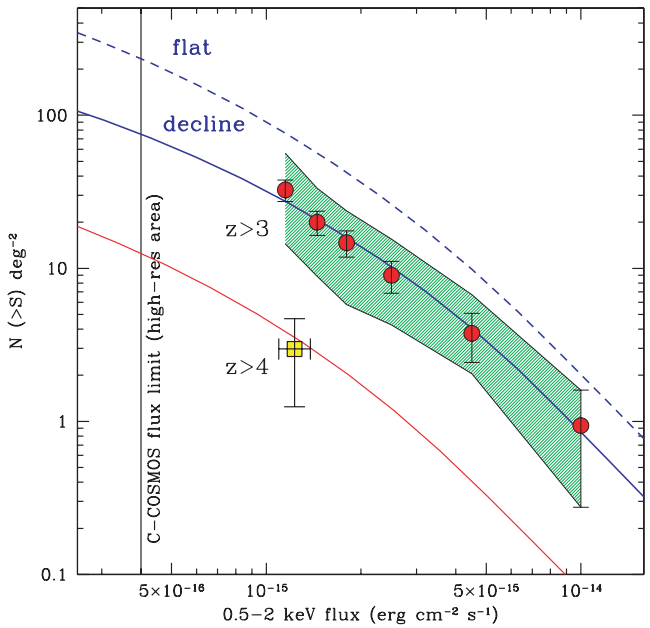

Figure 8. Binned log N–log S relation (red circles with associated Poissonian errors) of the $z > 3$ QSOs population. The dashed and solid blue curves correspond to two different predictions based on the Gilli et al. (2007) model. The former is obtained extrapolating the best-fit parameters of Hasinger et al. (2005) for the evolution of the X-ray LF to high-z, while an exponential decay at $z > 2.7$ is introduced in the latter. The green shaded area represents an estimate of the global error budget (see the text for details). The yellow square (with associated Poissonian error) is the estimate of the number counts for $z > 4$ quasars based on the four objects (three of them with a spectroscopic redshift) in the *XMM*–COSMOS sample. The red curve shows the predicted number counts assuming the exponential decay in the LF. The vertical line at 4×10^{-16} erg cm^{-2} s^{-1} represents the limit of the C-COSMOS survey.

(A color version of this figure is available in the online journal.)

redshift in X-ray-selected samples (e.g., Koekemoer et al. 2004; A. M. Koekemoer et al. 2009, in preparation). The dashed blue curve corresponds to the predictions of the XRB synthesis model (Gilli et al. 2007), obtained extrapolating to high-z the best-fit parameters of Hasinger et al. (2005), while the solid blue curve represents a model prediction obtained introducing in the LF an exponential decay with the same functional form ($\Phi(z) = \Phi(z_0) \times 10^{-0.43(z-z_0)}$) adopted by Schmidt et al. (1995) to fit the optical LF, corresponding to an e-folding per unit redshift.

The model predictions at $z > 3$ obtained extrapolating the Hasinger et al. (2005) best fit parameters (dashed line) clearly overestimate the observed counts even in the most optimistic scenario (upper boundary in Figure 8). A much better description to the observed counts is obtained by introducing the exponential decline in the X-ray LF with $z_0 = 2.7$ (following Schmidt et al. 1995).

An estimate of the number counts for $z >4$ QSOs is also shown in Figure 8. Although only four such objects are detected in the *XMM*–COSMOS survey, there is a remarkably good agreement with the predicted number counts, suggesting that the Schmidt et al. (1995) parameterization provides a good description of the X-ray-selected QSO surface densities up to $z \simeq 4.5$.

5.2. Comoving Space Densities

The comoving space density of $z > 3$ QSOs in three, almost equally populated, redshift bins ($z = 3.0$–4.5) is reported in Figure 9. The comoving space densities have been computed with the $1/V_{\rm max}$ method, originally proposed by Schmidt (1968), which takes into account the fact that more luminous objects are detectable over a larger volume. In order to reduce the effects of incompleteness (see Figure 5, right panel), the space densities have been computed for luminosities $\log L_X > 44.2$ (i.e., considering only 34 out of 39 objects). Because of the significant effects introduced by X-ray absorption, some particular care is needed in computing $V_{\rm max}$ for X-ray-selected sources. In fact, for any given intrinsic luminosity, the effective limiting flux for detecting obscured sources is higher than for unobscured ones and the corresponding volume over which obscured sources can be detected is smaller. We therefore calculate the maximum available volume for each source using the formula

$$V_{\rm max} = \int_{z_{\rm min}}^{z_{\rm max}} \Omega(f(L_x, z, N_H)) \frac{dV}{dz} dz,$$

where $\Omega(f(L_x, z))$ is the sky coverage at the flux $f(L_x, z)$ corresponding to a source with absorption column density N_H and unabsorbed luminosity L_X, and $z_{\rm max}$ is the maximum redshift at which the source can be observed at the flux limit of the survey.[19] More specifically, for unabsorbed sources we adopted the observed rest-frame 2–10 keV luminosity (see Section 4), while for obscured ones the unabsorbed luminosity was derived assuming the best fit column density as obtained from the HR. The limiting flux for each absorbed source was computed by folding the observed spectrum with the *XMM* sensitivity.

[19] If $z_{\rm max} > z_{\rm up,bin}$, then $z_{\rm max} = z_{\rm up,bin}$ where $z_{\rm up,bin}$ is the upper boundary of each redshift bin.

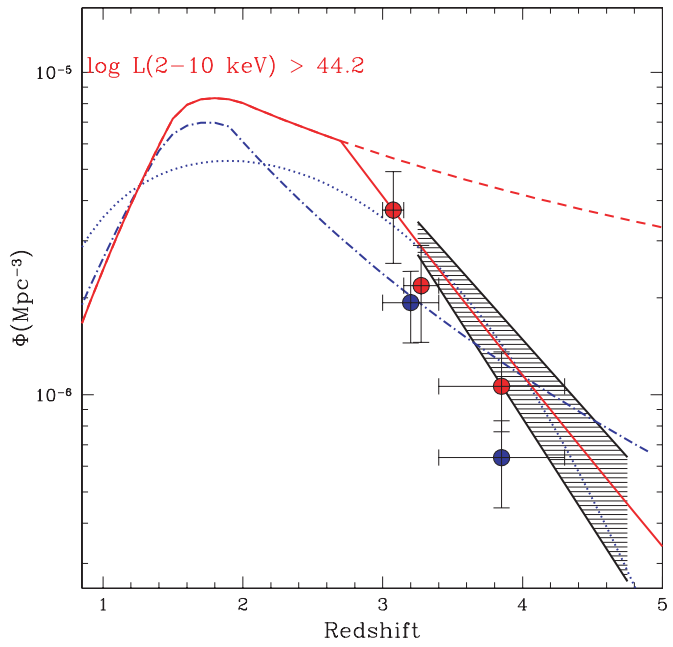

Figure 9. Comoving space density in three ($z = 3.0$–4.5) different redshift bins for the $z > 3$, $\log L_X > 44.2$ *XMM*–COSMOS sample. Red symbols (with associated errors) refer to the full sample (34 objects) and have been corrected for incompleteness against obscured sources (see the text for details). The red curve corresponds to the X-ray selected AGN space density computed for the same luminosity limit from the Gilli et al. (2007) model. At $z > 2.7$ we plot with two separate curves expectations when the exponential decline in the X-ray LF at $z > 2.7$ is introduced (continuous line) or not (dashed line, see the text for details). The dot-dashed and dotted lines correspond to the Silverman et al. (2008) LF, in the case of the LDDE and mod-PLE model, respectively (see Silverman et al. 2008 for details). Blue symbols (and associated errors) refer to the $i < 24$ sample (28 objects) and are corrected only for the volume effects to be compared with the Silverman et al. (2008) LF. The black shaded area represents the shape derived from brighter optical quasar, surveys (Schmidt et al. 1995 and Richards et al. 2006, upper and lower bounds respectively), rescaled up by an arbitrary factor ~ 80 for an easier comparison with the X-ray data.

(A color version of this figure is available in the online journal.)

For a proper comparison with model predictions at a given luminosity, we should also consider the population of obscured sources that are pushed below the limiting flux by the X-ray absorption, and correct the observed space density accordingly. In order to estimate the number of missed sources, we considered a population of luminous (intrinsic $\log L_x > 44.2$) obscured QSOs with the luminosity function and the column density distribution assumed by Gilli et al. (2007), and folded this population with the survey sky coverage. The results indicate that, at 0.5–2 keV fluxes larger than 10^{-15} erg cm^{-2} s^{-1}, about 25% and 45% of the full AGN population with intrinsic $\log L_X > 44.2$ are missing from our sample at a redshift of 3 and 4, respectively. For the computation of the space density we therefore weighted the contribution of each object taking into account the incompleteness toward the most obscured sources as a function of both redshift and source flux.

The space density of quasars with $\log L_X > 44.2$ from the full *XMM*–COSMOS $z > 3$ sample, corrected for the incompleteness against the most obscured sources as described above, is compared with the predictions from the Gilli et al. (2007) model at the same luminosity threshold (red dashed curve). Obscured, Compton thin AGNs are included following the prescriptions described above; Compton thick AGNs have not been included in the model given the fact that X-ray selection at the *XMM*–COSMOS limiting flux is insensitive to this population (see e.g., Tozzi et al. 2006). The red continuous line represents the expectations of the same model when the exponential decline in the X-ray LF discussed in Section 5.1 is introduced.

In agreement with the results obtained from the $\log N$–$\log S$, the declining space density provides an excellent representation of the observed data. Including the optically undetected sources in the $z > 3$ QSO sample, the space density of high-z QSOs would remain significantly below the extrapolation of the best-fit Hasinger et al. (2005) LF, although the shape of the observed decline would be different.

In order to compare our findings with the Silverman et al. (2008) recent estimates of the high-redshift LF, we have considered the same limit they adopted in the optical magnitude ($i < 24$) without correction for the incompleteness toward the most obscured sources. The blue symbols in Figure 9 are the space densities derived from the 28 objects at $I < 24$, computed correcting only for volume. The mod-PLE Silverman et al. (2008) LF is higher than our data over the entire redshift range ($3 < z < 4$); their LDDE LF is instead in very good agreement with our data point in the first redshift bin, while it is a factor of ~ 2 higher than our data at $z > 3.5$.

6. RESULTS AND DISCUSSION

The analysis of optical colors and X-ray spectra indicates that high redshift, X-ray-selected QSOs have optical properties not significantly different from those of optically selected, bright QSOs, even if a non-negligible fraction ($\sim$ 20%, i.e., the outliers of Figure 4) would not have been selected by the Casey et al. (2008) optical color–color criteria. Not surprisingly, these sources are optically faint and make up a significant fraction (30%) of the spectroscopically unidentified objects for which the observed HR does not allow us to constrain the column density.

Even if the bulk of the population of obscured AGNs responsible for the X-ray background is not fully sampled at the limiting flux of the *XMM*–COSMOS survey, the relative fraction ($\sim$ 20%) of obscured ($\log N_H > 23$) QSOs is not inconsistent, given the small number statistics, with that ($\sim$10%) predicted by Gilli et al. (2007). We note, moreover, that the $\log N_H > 23$ sample might be contaminated by less obscured sources ($\log N_H = 22$–23) given the relatively large errors associated with the measured HR. The depth of the *XMM*–COSMOS survey does not allow us to further investigate the absorption distribution for column densities lower than $\log N_H \simeq 23$, nor to firmly establish whether optically faint sources are X-ray obscured. The fraction of outliers in the optical color–color diagram is very similar to that of X-ray obscured sources and both are close to 20%. However, the two subsamples are marginally overlapping (only two optical outliers are also X-ray obscured) suggesting that gas absorption and dust reddening are not tightly correlated (see Maiolino et al. 2001).

The X-ray luminosity function of hard X-ray-selected AGNs as determined by combining several *Chandra* and *XMM* surveys (Ueda et al. 2003; La Franca et al. 2005) is well constrained up to relatively low redshifts ($z \sim 2$–3). At higher redshifts, the number statistics has so far prevented a robust estimate of their space density. Evidence for a decline at $z > 3$ was reported by Hasinger et al. (2005) and Silverman et al. (2005), but is limited to bright, unobscured QSOs. The $z > 3$ QSO sample drawn from the *XMM*–COSMOS survey allowed us, for the first time, to firmly address the issue of the evolution of high-redshift QSOs thanks to a homogeneous and sizable sample of X-ray sources much less biased against mildly obscured AGNs and with

an almost complete redshift information. The results indicate that the comoving space density of X-ray luminous ($L_X \gtrsim 10^{44}$ erg s^{-1}) QSOs at $z \sim 3$ is $(3.7 \pm 1.2) \times 10^{-6}$ Mpc^{-3} and declines exponentially (by an e-folding per unit redshift) in the $z \sim 3.0$–4.5 range. These results appear to be robust, despite the still remaining (small) uncertainties on the photometric redshifts discussed in Section 2.2. Moreover, if all the sources undetected in the optical band were at $z > 3$ equally populating the different redshift bins, the shape of the space density as a function of redshift would not change significantly. Only in the case that all the 10 optically undetected, soft X-ray sources turn out to be at $z >$3.5–4, the analytical parameterization of the observed decay should be modified.

The high-redshift decline is similar to that of luminous ($M_I < -27.6$), optically bright, unobscured QSOs, well established by SDSS observations (Richards et al. 2006), and can be satisfactorily described by the Schmidt et al. (1995) parameterization. Assuming an X-ray to optical spectral index appropriate for these luminosities ($\alpha_{ox} = -1.65$; e.g., Vignali et al. 2003; Steffen et al. 2006), the absolute magnitude SDSS limit corresponds to an X-ray luminosity $\log L_X \sim 45$. Therefore, the observed decline in the space density for the *XMM*–COSMOS sample strongly suggests that the evolution of mildly obscured (Compton thin) AGNs is very similar to that of unobscured, optically luminous QSOs, provided that the shape of the declining function holds also for luminosities which are about an order of magnitude lower than those probed by SDSS.

Silverman et al. (2008) computed the XLF for the optically bright ($i < 24$) X-ray population. Even though there is a good agreement at $z <$3.5 between their LDDE XLF and the observed *XMM*–COSMOS space densities (for the same limit in the optical magnitude), the extrapolation of their XLF at higher redshift is larger, by a factor of $\sim$ 2, than our data. A better fit would be obtained by tuning the Silverman et al. (2008) LF parameters responsible for the high redshift ($z >$ 3.0–3.5) behavior.

The observed decline in the comoving space density of X-ray-selected QSOs, at least for luminosities larger than $\sim 10^{44}$ erg s^{-1}, has a significant impact on the predictions of the QSOs number counts expected from future large area X-ray surveys, and, more in general, on predictions at all the wavelengths based on the current available XLF as representative of the high-redshift, radio-quiet population (e.g., Wilman et al. 2008). The present results may also provide a benchmark for theoretical models of SMBH growth. For example, the $z > 4$ QSOs number counts predicted by the Rhook & Haehnelt (2008) models (see central and right panels in their Figure 6) are about a factor of 7–8 higher than what is actually observed, suggesting that some of the model parameters should be revised.

The predicted number counts for a model with and without an exponential decline, at different limiting fluxes and redshift ranges are listed in Table 3. The *Chandra*–COSMOS survey provides a homogeneous coverage with high resolution (HPD $< 2''$) over the central ~ 0.5 deg^2 in COSMOS (M. Elvis et al. 2009, in preparation) down to a limiting flux of $\sim 4 \times 10^{-16}$ erg cm^{-2} s^{-1} in the 0.5–2 keV band (see vertical line in Figure 8). It will therefore roughly double the number of $z > 3$ quasars in that area, exploring the flux regime where the contribution from most obscured sources is higher.

As a practical example we also report the expectations for the extended ROentgen Survey with an Imaging Telescope Array (eROSITA; Predehl et al. 2007) survey with the Spectrum Röntgen Gamma (SRG) mission, which will be launched in the next few years. eROSITA will survey the entire extragalactic sky down to a limiting flux of $\sim 10^{-14}$ erg cm^{-2} s^{-1}in the 0.5–2 keV band. The number of expected $z > 3$ ($z > 4$) QSOs in the all sky survey, when the decline described in Section 5.2 is incorporated in our current knowledge of the XLF, is 2.5×10^4 (2100). eROSITA will also perform a deeper survey over an area of ~ 400 deg^2 down to a depth of 4×10^{-15} erg cm^{-2} s^{-1}. We expect to reveal $\sim$ 2500 QSOs at $z > 3$, about 200 of them at $z > 4$ and better constrain their redshift distribution.

Table 3
Expected Numbers of $z > 3$ QSOs in 0.5–2 keV Surveys

z Range	Limiting Flux (erg cm^{-2} s^{-1})	Constant[a] (deg^{-2})	Decline[b] (deg^{-2})
$z > 3$	$> 4 \times 10^{-16}$	230	75
	$> 10^{-15}$	80	30
	$> 4 \times 10^{-15}$	14	6.2
	$> 10^{-14}$	1.8	0.75
$z > 4$	$> 4 \times 10^{-16}$	80	12
	$> 10^{-15}$	30	7
	$> 4 \times 10^{-15}$	3	0.5
	$> 10^{-14}$	0.6	0.07

Notes.
[a] Predicted number counts assuming extrapolating the Hasinger et al. (2005) XLF at high redshifts.
[b] Predicted number counts assuming the Hasinger et al. (2005) XLF modified by an exponential decline at $z > 2.7$.

The study of QSOs space density and evolution at lower X-ray luminosities and higher redshifts requires much deeper observations. While a few moderately luminous ($\log L_X \sim$ 43–44), high redshift $z > 4$ quasars are detected in deep *Chandra* fields (i.e., Vignali et al. 2002) the present sample size is not such to constrain their space density. Additional high-z objects are expected to be revealed by ongoing ultra-deep *Chandra* (Luo et al. 2008) and *XMM-Newton* surveys.

7. SUMMARY

Taking advantage of the large area of the *XMM*–COSMOS survey and the associated deep multiwavelength follow-up, we have studied the physical and cosmological properties of $z >$ 3, X-ray-selected QSOs. This sample of 40 objects constitutes the largest and most complete (55% spectroscopic confirmation) sample of high-redshift quasars published so far and extracted from a single survey, at the depth of 10^{-15} erg cm^{-2} s^{-1} in the 0.5–2 keV band.

The most important results of our analysis can be summarized as follows.

1. X-ray-selected QSOs have optical properties which are not significantly different from those of optically selected (i.e., SDSS) objects.
2. From the analysis of X-ray colors and stacked spectra there is evidence of substantial X-ray absorption in about 20% of the sources.
3. There is no clear correlation between X-ray obscured sources and outliers in the Casey et al. (2008) optical color–color diagram; however, the outliers may contribute to the flatter X-ray spectrum observed for the spectroscopically unidentified objects for which the observed HR does not allow us to constrain the column density.
4. A steep decline in the space density of luminous X-ray-selected QSOs ($L_X > 10^{44.2}$ erg s^{-1}) at $z > 3$, similar to that observed for luminous optically selected quasars, is

needed to fit the observed data. This suggests that the high-redshift evolution of obscured AGNs is similar to that of unobscured ones.

We emphasize that, while the currently available XLF (e.g., Ueda et al. 2003; La Franca et al. 2005; Hasinger et al. 2005; Silverman et al. 2008) provide an excellent fit to the $z < 3$ redshift population, their extrapolations to high redshift would overpredict the present observational constraints by a factor ~ 2 at $z \sim 3$ and $\gtrsim 5$ at $z \sim 4$. As far as the luminous quasars are concerned ($\log L_X > 44.2$), a decay in their space density at $z \gtrsim 3$ should be included in the predictions of the high-z quasar population.

Future medium deep all sky X-ray surveys (e.g., eROSITA) with the associated multiwavelength follow-up will provide sizable samples ($> 10^4$) of $z > 3$ QSOs to further constrain the bright end of the QSO luminosity function. The evolution of the faint end of X-ray-selected QSO luminosity function up to very high redshift, $z \sim 6$ and perhaps beyond, will be investigated by future missions such as IXO (http://sci.esa.int/science-e/www/object/index.cfm?fobjectid=42271, http://ixo.gsfc.nasa.gov/) and Generation-X (Brissenden et al. 2008).

This work is based on observations obtained with *XMM-Newton*, an ESA Science Mission with instruments and contributions directly funded by ESA Member States and the USA (NASA). In Germany, the *XMM-Newton* project is supported by the Bundesministerium für Wirtschaft und Technologie/Deutsches Zentrum für Luft- und Raumfahrt (BMWI/DLR, FKZ 50 OX 0001), and the Max-Planck Society. M.B. acknowledges support from the *XMM-Newton* DLR grant 50-G-0502, G.H. acknowledges the contribution from the Leibniz Prize of the Deutsche Forschungsgemeinschaft under the grant HA 1850/28-1. In Italy, the *XMM*–COSMOS project is supported by ASI-INAF and PRIN/MIUR under grants I/023/05/00 and 2006–02–5203. The zCOSMOS ESO Large Program Number 175.A-0839 is acknowledged. These results are also based in part on observations obtained with the Walter Baade telescope of the Magellan Consortium at Las Campanas Observatory, and with the MMT which is operated by the MMT Observatory (MMTO), a joint venture of the Smithsonian Institution and the University of Arizona. We gratefully acknowledge the contributions of the entire COSMOS collaboration; more information on the COSMOS survey is available at http://www.astro.caltech.edu/ cosmos. This research has made use of the NASA/IPAC Extragalactic Database (NED) and the SDSS spectral archive. We thank the anonymous referee for his/her useful comments and suggestions.

REFERENCES

Adelman-McCarthy, J. K., et al. 2006, ApJS, 162, 38
Aird, J., Nandra, K., Georgakakis, A., Laird, E.S., Steidel, C.C., & Sharon, C. 2008, MNRAS, 387, 883
Alexander, D. M., Brandt, W. N., Hornschemeier, A. E., Garmire, G. P., Schneider, D. P., Bauer, F. E., & Griffiths, R. E. 2001, AJ, 122, 2156
Bongiorno, A., et al. 2007, A&A, 473, 443
Brandt, N. W., & Hasinger, G. 2005, ARA&A, 43, 827
Brissenden, R. J. V. and the Generation-X Team 2008, AAS/High-Energy Astrophys. Division, 10, 37.03
Brusa, M., et al. 2005, A&A, 432, 69
Brusa, M., et al. 2007, ApJS, 172, 353
Capak, P., et al. 2007, ApJS, 172, 99
Cappelluti, N., et al. 2007, ApJS, 172, 341
Casey, C. M., et al. 2008, ApJS, 177, 131
Cocchia, F., et al. 2007, A&A, 466, 31
Colless, M., et al. 2001, MNRAS, 328, 1039
Croom, S. M., Shanks, T., Boyle, B. J., Smith, R. J., Miller, L., Loaring, N. S., & Hoyle, F. 2001, MNRAS, 325, 483
Croom, S. M., Smith, R. J., Boyle, B. J., Shanks, T., Miller, L., Outram, P. J., & Loaring, N. S. 2005, MNRAS, 349, 1397
Di Matteo, T., Springel, V., & Hernquist, L. 2005, Nature, 433, 604
Fabian, A. C., & Iwasawa, K. 1999, MNRAS, 303L, 34
Fan, X., et al. 2001, AJ, 121, 54
Fan, X., et al. 2004, AJ, 128, 515
Ferrarese, L., & Merrit, D. 2000, ApJ, 539, L9
Finoguenov, A., et al. 2007, ApJS, 172, 182
Fiore, F., et al. 2003, A&A, 409, 79
Fiore, F., et al. 2008, ApJ, 672, 94
Fontanot, F., et al. 2007, A&A, 461, 39
Gallagher, S. C., Brandt, W. N., Chartas, G., & Garmire, G.P. 2002, ApJ, 567, 37
Gebhardt, K., et al. 2000, ApJ, 543, L5
Gilli, R., Comastri, A., & Hasinger, G. 2007, A&A, 463, 69
Hasinger, G. 2008, A&A, 490, 905
Hasinger, G., Miyaji, T., & Schmidt, M. 2005, A&A, 441, 417
Hasinger, G., et al. 2007, ApJS, 172, 29
Hopkins, P. F., Hernquist, L., Martini, P., Cox, T. J., Robertson, B., Di Matteo, T., & Springel, V. 2005, ApJ, 625, 71
Hunt, M. P., Steidel, C. C., Adelberger, K. L., & Shapley, A. E. 2004, ApJ, 605, 625
Kauffmann, G., et al. 2003, MNRAS, 346, 1055
Koekemoer, A. M., et al. 2004, ApJ, 600, L123
La Franca, F., et al. 2005, ApJ, 635, 864
Lapi, A., Shankar, F., Mao, J., Granato, G.L., Silva, L., De Zotti, G., & Danese, L. 2006, ApJ, 650, L42
Leauthaud, A., et al. 2007, ApJS, 172, 219
Lilly, S. J., et al. 2007, ApJS, 172, 70
Luo, B., et al. 2008, ApJS, 179, 19
Mainieri, V., et al. 2005, A&A, 437, 805
Mainieri, V., et al. 2007, ApJS, 172, 368
Maiolino, R., Marconi, A., Salvati, M., Risaliti, G., Severgnini, P., Oliva, E., La Franca, F., & Vanzi, L. 2001, A&A, 365, 28
Menci, N., Fiore, F., Puccetti, S., & Cavaliere, A. 2008, ApJ, 686, 219
Merloni, A., & Heinz, S. 2008, MNRAS, 388, 1011
Mignoli, M., et al. 2004, A&A, 418, 827
Norman, C., et al. 2002, ApJ, 571, 218
Predehl, P., et al. 2007, Proc. SPIE, 6686, 36
Prescott, M. K.M., Impey, C.D., Cool, R.J., & Scoville, N.Z. 2006, ApJ, 644, 100
Rhook, K. J., & Haehnelt, M. G. 2008, MNRAS, 389, 270
Richards, G., et al. 2006, AJ, 131, 2766
Salvato, M., et al. 2009, ApJ, 690, 1250
Sandage, A., & Wyndham, J.D. 1965, ApJ, 141, 328
Schmidt, M. 1968, ApJ, 151, 393
Schmidt, M., & Green, R.F. 1983, ApJ, 269, 352
Schmidt, M., Schneider, D.P., & Gunn, J.E. 1995, AJ, 110, 68
Scoville, N. Z., et al. 2007, ApJS, 172, 1
Shemmer, O., Brandt, W. N., Gallagher, S. C., Vignali, C., Boller, Th., Chartas, G., & Comastri, A. 2005, AJ, 130, 2522
Siana, B., et al. 2008, ApJ, 675, 49
Silverman, J. D., et al. 2005, ApJ, 624, 630
Silverman, J. D., et al. 2008, ApJ, 679, 118
Steffen, A. T., Strateva, I., Brandt, W. N., Alexander, D. M., Koekemoer, A. M., Lehmer, B. D., Schneider, D. P., & Vignali, C. 2006, AJ, 131, 2826
Steidel, C. C., Giaralisco, M., Pettini, M., Dickinson, M., & Adelberger, K. L. 1996, ApJ, 462, L17
Taniguchi, Y., et al. 2007, ApJS, 172, 9
Tozzi, P., et al. 2006, A&A, 451, 457
Treister, E., & Urry, C.M. 2005, ApJ, 630, 115
Treister, E., & Urry, C.M. 2006, ApJ, 652, L79
Trump, J. R., et al. 2007, ApJS, 172, 383
Trump, J. R., et al. 2009, ApJ, in press
Ueda, Y., Akiyama, M., Ohta, K., & Miyaji, T. 2003, ApJ, 598, 886
Vignali, C., Bauer, F.E., Alexander, D.M., Brandt, W.N., Hornschemeier, A.E., Schneider, D.P., & Garmire, G.P. 2002, ApJ, 580, L105
Vignali, C., Brandt, W.N., & Schneider, D.P. 2003, AJ, 125, 433
Volonteri, M., & Rees, M. 2006, ApJ, 650, 669
Wilman, R. J., et al. 2008, MNRAS, 388, 1335
Wolf, C., Wisotzki, L., Borch, A., Dye, S., Kleinheinrich, M., & Meisenheimer, K. 2003, A&A, 408, 499
Wolf, C., et al. 2004, A&A, 421, 913